

Quantum-metric-enabled exciton condensate in double twisted bilayer graphene

Xiang Hu,¹ Timo Hyart,^{2,3} Dmitry I. Pikulin,^{4,5} and Enrico Rossi¹

¹*Department of Physics, William & Mary, Williamsburg, VA 23187, USA*

²*International Research Centre MagTop, Institute of Physics,*

Polish Academy of Sciences, Aleja Lotnikow 32/46, PL-02668 Warsaw, Poland

³*Department of Applied Physics, Aalto University, 00076 Aalto, Espoo, Finland*

⁴*Microsoft Quantum, Redmond, Washington 98052, USA*

⁵*Microsoft Quantum, Station Q, Santa Barbara, California 93106-6105, USA*

(Dated: April 20, 2022)

Flat-band systems are a promising platform for realizing exotic collective ground states with spontaneously broken symmetry because the electron-electron interactions dominate over the kinetic energy. A collective ground state of particular interest is the chased after exciton condensate (EC). However, in flat band systems other collective ground states can compete with an EC phase, and the conventional treatment of the effect of thermal and quantum fluctuations predicts the EC phase should be unstable. Here, using double twisted bilayer graphene (TBLG) heterostructures as an example, we show that for realistic interaction strengths the EC phase is favored with respect to other TBLG's phases – orbital magnetism and superconductivity– when the TBLGs have opposite doping, and that the quantum metric of the Bloch wave functions stabilizes the EC, reversing the conclusion that would be drawn from the conventional approach in which quantum metric contributions are neglected. Our results suggest that the quantum metric plays a critical role in determining the stability of exciton condensates in double layers formed by systems with flat-bands.

An exciton is a bosonic quasiparticle formed by an electron (e) bound to a hole (h). A large number of excitons can become phase coherent and form a collective state known as exciton condensate (EC) [1, 2]. Already in the mid 70's it was proposed [3, 4] that spatially separating electrons and holes should facilitate the formation of a thermodynamically stable EC. Such separation can be realized in e-h semiconductor double layers, in which a thin dielectric separates the layers and distinct metal gates are used to create an excess density of electrons in one layer which equals the excess density of holes in the other one. Great advances in the fabrication of heterostructures made possible the realization of several novel double layers in which ECs could be realized [5–24]. It was proposed that ECs could be formed in graphene double layers [5, 6], but experimentally no strong signatures have been observed, so far. It was then proposed that ECs could be realized in systems based on double bilayer graphene (BLG) [8, 9, 16], given that at low energies BLG's bands are qualitatively flatter than graphene's, and recent experiments show signatures that are consistent with the formation of an EC [18]. These results, combined with the ones for quantum Hall (QH) bilayers [25–30], in which the kinetic term of each layer is completely quenched, would suggest that, in general, the formation of an EC is favored in bilayers formed by 2D systems with flat bands. As a consequence, double twisted bilayer graphene (TBLG), in which the bands can be made extremely flat by tuning the twist angle θ between graphene sheets [31–38] appears to be an ideal system to seek the realization of ECs without external magnetic fields. This expectation, however, is in part naive. First, the flatness of the bands is associated with strong screening of the interlayer Coulomb interaction that is the driver of the EC instability. This obstacle can be overcome by tuning the system into the strong coupling regime, where the e-(h-)densities are sufficiently small so that the coherence length ξ of the EC is smaller than the average

distance between particles [10]. Second, the stiffness (ρ_s) of the EC, i.e. its robustness against thermal and quantum fluctuations, is conventionally expected to decrease as the bands become flatter and ultimately vanish in the limit of perfectly flat bands.

In this work we show that the second obstacle in general might not be present if one considers the contribution to ρ_s due to the quantum metric of the eigenstates of the EC. We consider the specific case of double layers formed by an e-doped TBLG and a h-doped TBLG separated by a thin insulating barrier [Fig. 1(a)]. We first perform a mean field calculation, in which the order parameters for the EC, superconductivity (SC) and orbital magnetism (OM) are treated on equal footing, to identify the regions of the phase diagram as a function of dopings in the upper (U) and lower (L) TBLG where the EC is favored. We then calculate ρ_s for the EC and show that the contribution to it due to the quantum metric is essential to make it positive and therefore to stabilize the EC. In addition, we describe how ρ_s depends on the twist angle and find that the most favorable twist angle θ to realize a stable EC is not the magic angle. We also obtain the Berezinskii-Kosterlitz-Thouless (BKT) temperature T_{BKT} [39, 40] as function of θ . Considering that most systems with almost flat bands are multiband systems, our results have universal relevance for the understanding of the conditions necessary to realize ECs: they show that to realize an EC in 2D bilayers the flatness of the bands of the layers must be accompanied by a significant quantum metric contribution to the EC's stiffness. Our results also allow to understand in a new light the conditions that make possible the realization and observation of ECs in QH bilayers [41, 42].

The double TBLG system is described by the Hamiltonian $\hat{H} = \hat{H}^U + \hat{H}^L + \hat{H}_{\text{int}}$ where $\hat{H}^{U/L}$ is the single-particle Hamiltonian for the U/L TBLG and H_{int} describes the e-e interactions. We assume θ to be the same for the two

TBLGs. For small θ the low energy states of a TBLG are well described by an effective tight-binding Hamiltonian *in momentum space* with the lattice sites $\{\mathbf{b} = m_1 \mathbf{b}_1 + m_2 \mathbf{b}_2\}$ corresponding to the reciprocal lattice vectors of the moiré lattice. The on-site Hamiltonians describe the Dirac points of graphene with Fermi velocity $v_F = 10^6$ m/s, and the nearest-neighbor hopping matrices T_i describe the coupling between the layers with tunneling strength $w = 118$ meV [33, 43–45]. Here $\mathbf{b}_1 = (\sqrt{3}Q, 0)$, $\mathbf{b}_2 = (\sqrt{3}Q/2, 3Q/2)$, $m_1, m_2 \in \mathbb{Z}$, $Q = (8\pi/3a_0) \sin(\theta/2)$ and a_0 is the lattice constant of graphene. Recent experimental and theoretical results suggest that for a single TBLG the strongest instabilities are orbital-magnetism (OM), characterized by a finite polarization in sublattice space, and superconductivity (SC) [46–48]. We therefore decouple the interactions within the same TBLG via the mean fields $\Delta_{bl\sigma l'\sigma'}^{\text{OM,SC}} (l = l', \sigma = \sigma')$, where the indices l, l' (σ, σ') correspond to the layer (sublattice) degrees of freedom within the U or L TBLG [43]. The interaction between electrons in different TBLGs is decoupled via the EC mean field $\Delta_{bl\sigma l'\sigma'}^{\text{EC}}$. We assume the EC, SM, and OM phases obey the spin-rotation symmetry. Given the flatness of TBLG's low energy bands, in the mean-field approximation all the interactions can be replaced by effective *local* interactions [43]. We denote the strengths of the effective local interaction in the OM, SC and EC channels as V_{OM} , V_{SC} and V_{EC} , respectively. We expect $V_{\text{OM}} > V_{\text{SC}} \sim V_{\text{EC}}$, but it is challenging to estimate the precise values of the interaction strengths because of the interplay of screening effects and collective instabilities. Thus, we adopt a pragmatic approach: we set $V_{\text{OM}} = 130$ meV·nm², and $V_{\text{SC}} = 75$ meV·nm² so that the corresponding critical temperatures T_c^{OM} and T_c^{SC} are in good agreement with the experimental observations [34, 37], and consider different range of values for V_{EC} , 60 – 100 meV·nm², for which $T_c^{\text{EC}} \sim 1 - 4$ K, and the system is in a strong coupling regime where the screening does not prevent the formation of the EC.

The gap equations for each order parameter (OP) $\Delta_{\bar{\alpha}}^{\text{OP}}$, where $\text{OP} = \{\text{OM}, \text{SC}, \text{EC}\}$, and $\bar{\alpha}$ is a collective index, can be linearized close to the critical temperature T_c^{OP} : $\Delta_{\bar{\alpha}}^{\text{OP}} = \sum_{\bar{\beta}} \chi_{\bar{\alpha}\bar{\beta}}^{\text{OP}} \Delta_{\bar{\beta}}^{\text{OP}}$, where $\chi_{\bar{\alpha}\bar{\beta}}^{\text{OP}}$ is the bare susceptibility, independent of $\Delta_{\bar{\alpha}}^{\text{OP}}$. T_c^{OP} is obtained as the temperature T for which the largest eigenvalue of $\chi_{\bar{\alpha}\bar{\beta}}^{\text{OP}}$ is equal to 1. The expressions of $\chi_{\bar{\alpha}\bar{\beta}}^{\text{OP}}$ for each phase are given in [43]. In Fig. 1(b) we show the phase diagram, as function of doping in each TBLG, for $V_{\text{EC}} = 60$ meV·nm², obtained by identifying the highest T_c^{OP} . We have verified for several (μ_U, μ_L) value pairs that the results obtained from the linearized and non-linearized gap equations are consistent. Close to $\nu_U = \nu_L = 0$ the correlated insulating phase OM is favored, whereas introducing equal electron densities in the two TBLGs $\mu_L \sim \mu_U$ favors the SC phase [49]. When the excess density of electrons in one TBLG equals the excess density of holes in the other TBLG, $\mu_U \sim -\mu_L$, the EC becomes dominant. In our system the EC is formed by states in physically different TBLGs, no pairing between states in bands with opposite Chern number is as-

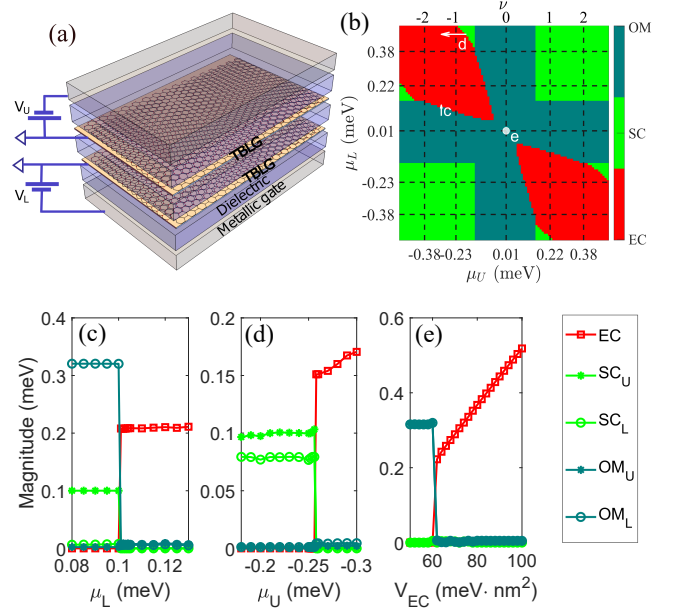


FIG. 1. (a) Proposed experimental setup. (b) Phase diagram of double-TBLG as a function of μ_U and μ_L for $\theta = 1.00^\circ$. (c,d) Phase transitions as a function of dopings along the arrows shown in (b). (e) Phase transition as a function of V_{EC} at $\nu_U = \nu_L = 0$. The legend $\text{SC}(\text{OM})_{\text{U(L)}}$ represents the SC (OM) phase in the Upper (Lower) TBLG.

sumed, and so the topology of the low energy bands does not penalize the formation of a uniform *inter-TBLG* EC state [50].

To investigate the possible coexistence of ordered phases [51] we have solved across several phase boundaries the full non-linear gap equations in which all the order parameters are allowed to be nonzero. We used large numbers of random initial conditions and identified the solution with the smallest total energy as the ground state. Fig. 1 (c) and (d) show the evolution of the order parameters across the OM/EC and SC/EC phase boundaries, respectively. In both cases the results suggest that the system undergoes a first-order quantum phase transition as the dopings are varied in Fig. 1(b). Fig. 1(e) shows the evolution of the order parameters as a function of V_{EC} at the neutrality point. Also in this case the transition appears to be first order. Figure 1(e) suggest that for $V_{\text{EC}} > 60$ meV·nm² the EC is favored in a significant region of the (μ_U, μ_L) plane. In the remainder we focus on the $\mu_L = -\mu_U \equiv \mu$ regime, with μ sufficiently large, and set $V_{\text{EC}} = 100$ meV·nm² so that, at the mean-field level, the EC phase is dominant. To simplify the notation in the sections below the EC label is implied.

Fig. 2 shows how T_c scales with μ and θ close to the magic angle $\theta_M = 1.05^\circ$. T_c is largest when $\theta = \theta_M$, twist angle for which the bands are flattest, and decreases quickly when θ is tuned away from θ_M . The solution of the gap equation reveals that $\Delta_{bl\sigma l'\sigma'}$ has several non-zero components. We performed the singular value decomposition (SVD), $\Delta_{bl\sigma l'\sigma'} = USV^\dagger$, where S is a diagonal matrix whose diagonal elements are the *singular values* of $\Delta_{bl\sigma l'\sigma'}$. Fig. 3(a) shows that the largest 20

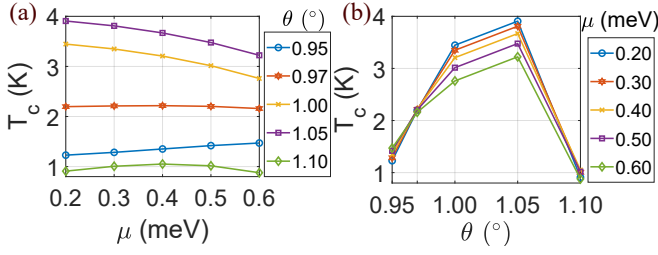


FIG. 2. (a) T_c as a function of $\mu = \mu_L = -\mu_U$ and different values of twist angle θ . (b) T_c as a function of θ and different values of μ .

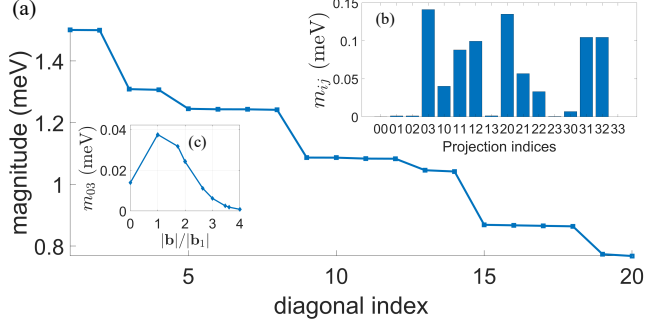


FIG. 3. (a) The first twenty singular values of the SVD decomposition $\Delta_{\mathbf{b}l\sigma'l'\sigma'} = USV^\dagger$. (b) Amplitudes of the order parameter components m_{ij} . (c) Scaling with $|b|$ of m_{03} . Here $\theta = 1.05^\circ$ and $\mu = 0.30$ meV.

singular values (in total we have 484 singular values [43]) are of comparable size confirming the multi-component nature of the order parameter.

To better understand the orbital structure of $\Delta_{\mathbf{b}l\sigma'l'\sigma'}$ we calculated its projections on the 4×4 matrices $\kappa_i \otimes \sigma_j$ as $m_{ij} = [\sum_{\mathbf{b}} \|a_{ij}^{(\mathbf{b})}\|^2]^{1/2}$, $a_{ij}^{(\mathbf{b})} = (1/4)\text{Tr}[\Delta_{\mathbf{b}l\sigma'l'\sigma'} \kappa_i \otimes \sigma_j]$, where κ_i (σ_i) are the Pauli matrices in the layer (sublattice) space. We see, Fig. 3 (b), that m_{03} is the largest projection, but several other projections are comparable to it. The fairly even distribution of the EC's order parameter over different orbital channels is paralleled by its fairly slow decay with $|b|$, see Fig. 3(c). These results are consistent with the SVD's result that $\Delta_{\mathbf{b}l\sigma'l'\sigma'}$ describes a multi-component order parameter. This is in contrast with the results for the case of superconducting pairing in isolated TBLG where the pairing is dominated by a single channel and the magnitude of the order parameter decreases quickly with $|b|$ [48, 52].

Fig. 4 shows the low energy bands along the $\gamma - \kappa_+ - \nu - \gamma - \bar{\nu}$ path in the moiré Brillouin zone (BZ) [43] for $\theta = 1.05^\circ$, and $\theta = 1.00^\circ$, in the presence of the EC condensate. For $\theta = 1.05^\circ$ the very large Fermi velocity of the low energy bands at the γ point prevents the EC from opening a gap at this point. As θ is tuned away from θ_M the singularity at the γ point morphs into two very small e-h pockets, Fig. 4(b). The results of Fig. 4(a,b) show that in double layer TBLG the EC is expected to be, strictly speaking, gapless. However, given

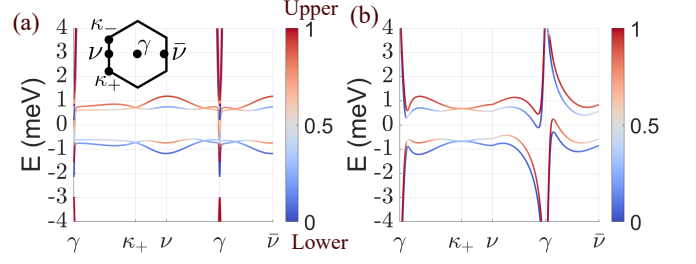


FIG. 4. Band structures in the EC phase at $T = 0$ and $\mu = 0.30$ meV for (a) $\theta = 1.05^\circ$ and (b) $\theta = 1.00^\circ$. The colorbar indicates how much the eigenstate is localized in the U/L TBLG. The inset in (a) shows the moiré Brillouin zone.

that the gapless nature is due to a very small number of states close to a single point of the BZ, the density of states is very negligible within the EC's gap (see [43]), and so we expect that the transition to the EC state could be clearly observed in transport and spectroscopy measurements.

We now consider the stability of the EC with respect to fluctuations. The dominant fluctuations are the ones of the phase, $\varphi(\mathbf{r})$, of the order parameter: $\Delta \rightarrow \Delta e^{i\varphi(\mathbf{r})}$. Expanding the action in the long-wavelength limit around the saddle point identified by the mean-field solution we have $S = S_0 + \int d\tau \int d\mathbf{r} \frac{1}{2} \rho_{\alpha\beta}^s \partial_{r_\alpha} \varphi \partial_{r_\beta} \varphi$, where S_0 is the action at the saddle point, and $\rho_{\alpha\beta}^s$ is the $\alpha\beta$ component of the EC's stiffness. The EC is stable when $\rho_{\alpha\beta}^s$ is positive-definite. For a multiband system $\rho_{\alpha\beta}^s$ is given by the general expression [53, 54]:

$$\rho_{\alpha\beta}^s = \sum_{\mathbf{k}, i, j} \frac{n_F(E_j) - n_F(E_i)}{E_i - E_j} \left(\frac{1}{4A} \langle \psi_i | \hat{v}_{\alpha} | \psi_j \rangle \langle \psi_j | \hat{v}_{\beta} | \psi_i \rangle - \frac{1}{A} \langle \psi_i | \hat{v}_{cf, \alpha} | \psi_j \rangle \langle \psi_j | \hat{v}_{cf, \beta} | \psi_i \rangle \right), \quad (1)$$

where E_i ($|\psi_i\rangle$) are the eigenvalues (eigenstates) of the mean-field Hamiltonian H_{MF} , $n_F(E)$ is the Fermi-Dirac distribution, A is the area of the sample, $\hat{v}_{\alpha}(\mathbf{k}) = \partial H_{\text{MF}} / \partial k_{\alpha}$ and $\hat{v}_{cf, \alpha}(\mathbf{k}) = (1/2)\gamma_z \partial H_{\text{MF}} / \partial k_{\alpha}$ are the components of the regular and counterflow velocity operators, respectively, γ_z is the Pauli matrix acting in the U/L subspace, and $\mathbf{k} = (k_x, k_y)$ is the Bloch wave vector. In our case, $\rho_{xy}^s = \rho_{yx}^s = 0$, and $\rho_{xx}^s = \rho_{yy}^s \equiv \rho_s$. For a multi-band system we can identify a conventional contribution, to ρ_s , ρ_s^{conv} , arising almost exclusively from intraband terms (*same band index in the electron or hole subspace*), and a "geometric" contribution, ρ_s^{geom} , due to interband terms (*different band indexes in both the electron and hole subspaces*), and write $\rho^s = \rho_s^{\text{conv}} + \rho_s^{\text{geom}}$. Because ρ_s^{geom} is closely connected to the quantum metric of the Hilbert space spanned by the eigenstates of H_{MF} [52–57], it is often called a geometric contribution to the superfluid stiffness.

Fig 5 shows how ρ_s^{conv} , ρ_s^{geom} and ρ^s depend on μ and θ . All the results were obtained for $\mathcal{T} = 20$ mK $\ll T_c$. We notice that ρ_s does not grow with μ contrary to the conventional

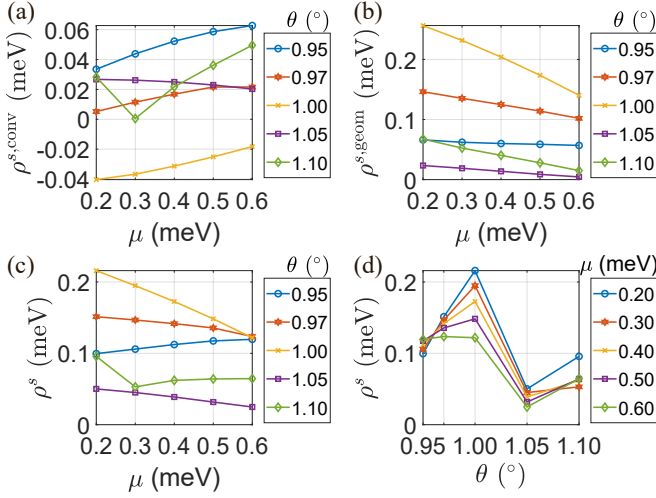


FIG. 5. (a) Conventional $\rho^{s,\text{conv}}$, (b) geometric $\rho^{s,\text{geom}}$, and (c) total stiffness ρ^s as a function of μ for different values of θ . (d) ρ^s vs. θ for different values of μ .

result $\rho_s \propto \mu$. For $\theta = 1.05^\circ$, and $\theta = 1.10^\circ$, $\rho^{s,\text{conv}}$ and $\rho^{s,\text{geom}}$ are comparable and the relative weight changes with μ . For all the other twist angles considered $\rho^{s,\text{geom}}$ is larger than $\rho^{s,\text{conv}}$, regardless of μ .

The results of Fig. 2 (a) show that the mean field critical temperature T_c at $\theta = 1.00^\circ$ is only slightly smaller than at $\theta = \theta_M$, and therefore that, at the mean-field level, double-layer TBLG with $\theta = 1.00^\circ$ is a very good candidate for the realization of an EC. However, strikingly, for $\theta = 1.00^\circ$ we find that $\rho^{s,\text{conv}}$ for the EC is negative for all the values of μ , see Fig. 5 (a) (this can happen because of the lack of particle-hole symmetry). This result would lead us to conclude that for $\theta = 1.00^\circ$ the EC is fragile against fluctuations and therefore not a stable ground state, despite the relatively large value of T_c . This conclusion is reversed if one takes into account the geometric contribution to ρ_s , Fig. 5 (b): for $\theta = 1.00^\circ$ the $\rho^{s,\text{geom}}$ is positive and much larger, in absolute value, than $\rho^{s,\text{conv}}$, guaranteeing the robust stability of the EC. In fact, Figs. 5 (c), (d) allow us to conclude that the EC is most stable for $\theta = 1.00^\circ$, not for $\theta = \theta_M$ as one would infer from the mean-field results.

The results of Fig. 5(c),(d) can be used to obtain T_{BKT} , via the equation $k_B T_{\text{BKT}} = 2\pi\rho^s[\Delta(T_{\text{BKT}}), T_{\text{BKT}}]$, where we have taken into account the valley and spin degeneracies. For the dependence of Δ on \mathcal{T} we can adopt the BCS scaling $\Delta(\mathcal{T}) = 1.764k_B T_c (1 - \mathcal{T}/T_c)^{1/2}$, with k_B the Boltzmann's constant. The results for T_{BKT} are shown in Fig. 6. From Fig. 6 (a), (b) we see that, contrary to the mean-field results, the twist angle for which the critical temperature T_{BKT} is largest is not θ_M , but $\theta = 1.00^\circ$, for all the values of μ . Indeed T_{BKT} at $\theta = 1.00^\circ$ is up to 50% larger than at θ_M . This somewhat surprising result arises entirely from the geometric contribution to ρ_s . It is interesting to notice that, contrary to the conventional wisdom, for some twist angles T_{BKT} de-

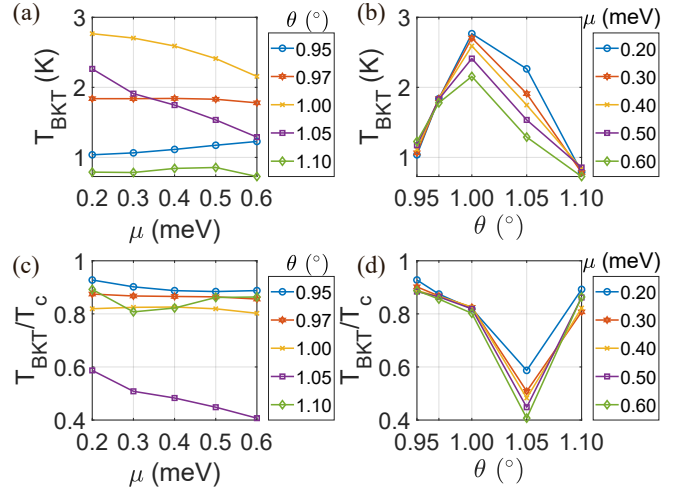


FIG. 6. (a) T_{BKT} as a function of μ for different values of θ . (b) T_{BKT} as a function of θ for different values of μ . (c), (d) T_{BKT}/T_c as a function of μ, θ , respectively.

creases, rather than increasing, with μ . Such behavior is particularly marked for $\theta = 1.00^\circ$ and $\theta = \theta_M$, Fig. 6 (a), due to the significant decrease of the geometric contribution to ρ_s , as seen in Fig. 5. Figures 6 (c), (d) show how the ratio T_{BKT}/T_c scales with μ and θ , respectively. It is particularly interesting to see that, for all values of μ , T_{BKT}/T_c is minimum at θ_M .

In summary, we have studied the competition between OM, SC and EC phases as a function of the dopings of the layers via comprehensive mean-field calculations in double TBLG systems. We have discussed the nature of the phase transitions, and we have shown that for realistic interaction strengths the EC phase is favored when the TBLGs have sufficiently large and opposite dopings. We then studied the stiffness ρ_s of the EC and demonstrated that the quantum metric contribution to ρ_s is essential to make ρ_s positive so that the EC is stable against fluctuations. A ‘‘conventional’’ study of the EC’s stability that does not include interbands terms would lead to the conclusion that in flat-band double layers ECs can be unstable. However, we found that this conclusion is reversed if the interband terms responsible for the quantum metric of the flat bands are taken into account. Finally, we obtained T_{BKT} for the ECs and found that the largest T_{BKT} is realized not at the magic angle, $\theta = 1.05^\circ$, but at $\theta = 1.00^\circ$. The results present a comprehensive and detailed picture of the possible correlated states of double-twisted bilayer graphene, and show the role played by the quantum metric on the stability and T_{BKT} of the exciton condensate in double-twisted bilayer graphene and so should constitute a useful guide to experimentalists studying the correlated phases of these novel systems. In a more general context, our findings point to the importance of the quantum metric for the understanding of the physics of ECs in flat band systems, including QH and moiré bilayers [58–60].

X.H and E.R. acknowledge support from ARO (Grant No.

W911NF-18-1-0290) and NSF (Grant No. DMR- 1455233). E.R. also thanks the Aspen Center for Physics, which is supported by NSF Grant No. PHY-1607611, and KITP, supported by Grant No. NSF PHY1748958, where part of this work was performed. X.H. acknowledge the hospitality of Hunan Normal University. The authors acknowledge William & Mary Research Computing for providing computational resources. Part of the calculations were performed on the Extreme Science and Engineering Discovery Environment (XSEDE) [61] Stampede2 at TACC through allocation TG-PHY210052. The research was partially supported by the Foundation for Polish Science through the IRA Programme co-financed by EU within SG OP.

-
- [1] L. V. Keldysh and Y. E. Kopaev, Possible instability of the semimetallic state toward Coulomb interaction, *Sov. Phys. Solid State* **6**, 2219 (1965).
- [2] B. Halperin and T. Rice, The excitonic state at the semiconductor-semimetal transition (Academic Press, 1968) pp. 115 – 192.
- [3] Y. E. Lozovik and V. I. Yudson, Feasibility of superfluidity of paired spatially separated electrons and holes - new superconductivity mechanism, *Jetp Lett.* **22**, 274 (1975).
- [4] Y. E. Lozovik and V. I. Yudson, Novel mechanism of superconductivity - pairing of spatially separated electrons and holes, *Zhurnal Eksperimentalnoi I Teoreticheskoi Fiziki* **71**, 738 (1976).
- [5] H. Min, R. Bistritzer, J.-J. Su, and A. H. MacDonald, Room-temperature superfluidity in graphene bilayers, *Phys. Rev. B* **78**, 121401(R) (2008).
- [6] C. Zhang and Y. N. Joglekar, Excitonic condensation of massless fermions in graphene bilayers, *Phys. Rev. B* **77**, 233405 (2008).
- [7] M. Y. Kharitonov and K. B. Efetov, Electron screening and excitonic condensation in double-layer graphene systems, *Physical Review B* **78**, 241401(R) (2008).
- [8] J. Zhang and E. Rossi, Chiral superfluid states in hybrid graphene heterostructures, *Phys. Rev. Lett.* **111**, 086804 (2013).
- [9] A. Perali, D. Neilson, and A. R. Hamilton, High-temperature superfluidity in double-bilayer graphene, *Phys. Rev. Lett.* **110**, 146803 (2013).
- [10] D. Neilson, A. Perali, and A. R. Hamilton, Excitonic superfluidity and screening in electron-hole bilayer systems, *Phys. Rev. B* **89**, 060502(R) (2014).
- [11] D. I. Pikulin and T. Hyart, Interplay of exciton condensation and the quantum spin hall effect in InAs/GaSb bilayers, *Phys. Rev. Lett.* **112**, 176403 (2014).
- [12] M. M. Fogler, L. V. Butov, and K. S. Novoselov, High-temperature superfluidity with indirect excitons in van der Waals heterostructures, *Nature Communications* **5**, 4555 (2014).
- [13] D. I. Pikulin, P. G. Silvestrov, and T. Hyart, Confinement-deconfinement transition due to spontaneous symmetry breaking in quantum Hall bilayers, *Nature Communications* **7**, 10462 (2016).
- [14] J. I. A. Li, T. Taniguchi, K. Watanabe, J. Hone, and C. R. Dean, Excitonic superfluid phase in double bilayer graphene, *Nature Physics* **13**, 751 (2017).
- [15] B. Debnath, Y. Barlas, D. Wickramaratne, M. R. Neupane, and R. K. Lake, Exciton condensate in bilayer transition metal dichalcogenides: Strong coupling regime, *Physical Review B* **96**, 174504 (2017).
- [16] J.-J. Su and A. H. MacDonald, Spatially indirect exciton condensate phases in double bilayer graphene, *Phys. Rev. B* **95**, 045416 (2017).
- [17] L. Du, X. Li, W. Lou, G. Sullivan, K. Chang, J. Kono, and R.-R. Du, Evidence for a topological excitonic insulator in InAs/GaSb bilayers, *Nature Communications* **8**, 1971 (2017).
- [18] G. W. Burg, N. Prasad, K. Kim, T. Taniguchi, K. Watanabe, A. H. MacDonald, L. F. Register, and E. Tutuc, Strongly enhanced tunneling at total charge neutrality in double-bilayer graphene-WSe₂ heterostructures, *Phys. Rev. Lett.* **120**, 177702 (2018).
- [19] K. Tran, G. Moody, F. Wu, X. Lu, J. Choi, K. Kim, A. Rai, D. A. Sanchez, J. Quan, A. Singh, J. Embley, A. Zepeda, M. Campbell, T. Autry, T. Taniguchi, K. Watanabe, N. Lu, S. K. Banerjee, K. L. Silverman, S. Kim, E. Tutuc, L. Yang, A. H. MacDonald, and X. Li, Evidence for moiré excitons in van der Waals heterostructures, *Nature* **567**, 71 (2019).
- [20] Z. Wang, D. A. Rhodes, K. Watanabe, T. Taniguchi, J. C. Hone, J. Shan, and K. F. Mak, Evidence of high-temperature exciton condensation in two-dimensional atomic double layers, *Nature* **574**, 76 (2019).
- [21] X. Liu, Z. Hao, K. Watanabe, T. Taniguchi, B. I. Halperin, and P. Kim, Interlayer fractional quantum Hall effect in a coupled graphene double layer, *Nature Physics* **15**, 893 (2019).
- [22] Y. H. Kwan, Y. Hu, S. H. Simon, and S. A. Parameswaran, Excitonic fractional quantum Hall hierarchy in moiré heterostructures, [arXiv:2003.11559](https://arxiv.org/abs/2003.11559) (2020).
- [23] Y. H. Kwan, Y. Hu, S. H. Simon, and S. A. Parameswaran, Exciton band topology in spontaneous quantum anomalous hall insulators: Applications to twisted bilayer graphene, *Phys. Rev. Lett.* **126**, 137601 (2021).
- [24] Y. Shimazaki, I. Schwartz, K. Watanabe, T. Taniguchi, M. Kroner, and A. Imamoğlu, Strongly correlated electrons and hybrid excitons in a moiré heterostructure, *Nature* **580**, 472 (2020).
- [25] I. B. Spielman, J. P. Eisenstein, L. N. Pfeiffer, and K. W. West, Resonantly Enhanced Tunneling in a Double Layer Quantum Hall Ferromagnet, *Physical Review Letters* **84**, 5808 (2000).
- [26] A. Stern, S. M. Girvin, A. H. MacDonald, and N. Ma, Theory of interlayer tunneling in bilayer quantum hall ferromagnets, *Phys. Rev. Lett.* **86**, 1829 (2001).
- [27] J. P. Eisenstein and A. H. MacDonald, Bose–Einstein condensation of excitons in bilayer electron systems, *Nature* **432**, 691 (2004).
- [28] E. Rossi, A. S. Núñez, and A. H. MacDonald, Interlayer Transport in Bilayer Quantum Hall Systems, *Physical Review Letters* **95**, 266804 (2005).
- [29] A. D. K. Finck, J. P. Eisenstein, L. N. Pfeiffer, and K. W. West, Exciton Transport and Andreev Reflection in a Bilayer Quantum Hall System, *Physical Review Letters* **106**, 236807 (2011).
- [30] T. Hyart and B. Rosenow, Quantitative description of Josephson-like tunneling in $\nu_T = 1$ quantum Hall bilayers, *Physical Review B* **83**, 155315 (2011).
- [31] J. M. B. Lopes dos Santos, N. M. R. Peres, and A. H. Castro Neto, Graphene bilayer with a twist: Electronic structure, *Phys. Rev. Lett.* **99**, 256802 (2007).
- [32] E. Suárez Morell, J. D. Correa, P. Vargas, M. Pacheco, and Z. Barticevic, Flat bands in slightly twisted bilayer graphene: Tight-binding calculations, *Physical Review B* **82**, 121407(R) (2010).
- [33] R. Bistritzer and A. H. MacDonald, Moire bands in twisted double-layer graphene, *Proceedings of the National Academy*

- of Sciences **108**, 12233 (2011).
- [34] Y. Cao, V. Fatemi, S. Fang, K. Watanabe, T. Taniguchi, E. Kaxiras, and P. Jarillo-Herrero, Unconventional superconductivity in magic-angle graphene superlattices, *Nature* **556**, 43 (2018).
- [35] Y. Cao, V. Fatemi, A. Demir, S. Fang, S. L. Tomarken, J. Y. Luo, J. D. Sanchez-Yamagishi, K. Watanabe, T. Taniguchi, E. Kaxiras, R. C. Ashoori, and P. Jarillo-Herrero, Correlated insulator behaviour at half-filling in magic-angle graphene superlattices, *Nature* **556**, 80 (2018).
- [36] M. Yankowitz, S. Chen, H. Polshyn, Y. Zhang, K. Watanabe, T. Taniguchi, D. Graf, A. F. Young, and C. R. Dean, Tuning superconductivity in twisted bilayer graphene, *Science* **363**, 1059 (2019).
- [37] X. Lu, P. Stepanov, W. Yang, M. Xie, M. A. Aamir, I. Das, C. Urgell, K. Watanabe, T. Taniguchi, G. Zhang, A. Bachtold, A. H. MacDonald, and D. K. Efetov, Superconductors, orbital magnets and correlated states in magic-angle bilayer graphene, *Nature* **574**, 653 (2019).
- [38] E. Y. Andrei and A. H. MacDonald, Graphene bilayers with a twist, *Nature Materials* **19**, 1265 (2020).
- [39] V. L. Berezinskiĭ, Destruction of Long-range Order in One-dimensional and Two-dimensional Systems having a Continuous Symmetry Group I. Classical Systems, *Soviet Journal of Experimental and Theoretical Physics* **32**, 493 (1971).
- [40] J. M. Kosterlitz and D. J. Thouless, Ordering, metastability and phase transitions in two-dimensional systems, *Journal of Physics C: Solid State Physics* **6**, 1181 (1973).
- [41] K. Yang, K. Moon, L. Zheng, A. H. MacDonald, S. M. Girvin, D. Yoshioka, and S.-C. Zhang, Quantum ferromagnetism and phase transitions in double-layer quantum hall systems, *Phys. Rev. Lett.* **72**, 732 (1994).
- [42] K. Moon, H. Mori, K. Yang, S. M. Girvin, A. H. MacDonald, L. Zheng, D. Yoshioka, and S.-C. Zhang, Spontaneous interlayer coherence in double-layer quantum hall systems: Charged vortices and kosterlitz-thouless phase transitions, *Phys. Rev. B* **51**, 5138 (1995).
- [43] Supplementary material, which includes Refs. [13, 33, 42, 44–46, 48, 49, 51, 62–65]
- [44] J. Jung, A. Raoux, Z. Qiao, and A. H. MacDonald, Ab initio theory of moiré superlattice bands in layered two-dimensional materials, *Phys. Rev. B* **89**, 205414 (2014).
- [45] S. Carr, S. Fang, P. Jarillo-Herrero, and E. Kaxiras, Pressure dependence of the magic twist angle in graphene superlattices, *Physical Review B* **98**, 085144 (2018).
- [46] M. Xie and A. H. Macdonald, Nature of the Correlated Insulator States in Twisted Bilayer Graphene, *Physical Review Letters* **124**, 097601 (2020).
- [47] T. J. Peltonen, R. Ojajarvi, and T. T. Heikkilä, Mean-field theory for superconductivity in twisted bilayer graphene, *Phys. Rev. B* **98**, 220504(R) (2018).
- [48] F. Wu, A. H. MacDonald, and I. Martin, Theory of Phonon-Mediated Superconductivity in Twisted Bilayer Graphene, *Physical Review Letters* **121**, 257001 (2018).
- [49] T. Löthman and A. M. Black-Schaffer, Universal phase diagrams with superconducting domes for electronic flat bands, *Phys. Rev. B* **96**, 064505 (2017).
- [50] N. Bultinck, S. Chatterjee, and M. P. Zaletel, Mechanism for Anomalous Hall Ferromagnetism in Twisted Bilayer Graphene, *Phys. Rev. Lett.* **124**, 166601 (2020).
- [51] R. Ojajarvi, T. Hyart, M. A. Silaev, and T. T. Heikkilä, Competition of electron-phonon mediated superconductivity and Stoner magnetism on a flat band, *Phys. Rev. B* **98**, 054515 (2018).
- [52] X. Hu, T. Hyart, D. I. Pikulin, and E. Rossi, Geometric and conventional contribution to the superfluid weight in twisted bilayer graphene, *Phys. Rev. Lett.* **123**, 237002 (2019).
- [53] S. Peotta and P. Törmä, Superfluidity in topologically nontrivial flat bands, *Nature Communications* **6**, 8944 (2015).
- [54] L. Liang, T. I. Vanhala, S. Peotta, T. Siro, A. Harju, and P. Törmä, Band geometry, Berry curvature, and superfluid weight, *Phys. Rev. B* **95**, 024515 (2017).
- [55] F. Xie, Z. Song, B. Lian, and B. A. Bernevig, Topology-bounded superfluid weight in twisted bilayer graphene, *Phys. Rev. Lett.* **124**, 167002 (2020).
- [56] A. Julku, T. J. Peltonen, L. Liang, T. T. Heikkilä, and P. Törmä, Superfluid weight and Berezinskii-Kosterlitz-Thouless transition temperature of twisted bilayer graphene, *Phys. Rev. B* **101**, 060505(R) (2020).
- [57] J. Cao, H. A. Fertig, and L. Brey, Quantum geometric exciton drift velocity, *Phys. Rev. B* **103**, 115422 (2021).
- [58] Q. Shi, E.-M. Shih, D. Rhodes, B. Kim, K. Barmak, K. Watanabe, T. Taniguchi, Z. Papić, D. A. Abanin, J. Hone, and C. R. Dean, Bilayer wse₂ as a natural platform for interlayer exciton condensates in the strong coupling limit (2021), [arXiv:2108.10477 \[cond-mat.mes-hall\]](https://arxiv.org/abs/2108.10477).
- [59] J. Jang, H. M. Yoo, L. N. Pfeiffer, K. W. West, K. W. Baldwin, and R. C. Ashoori, Strong interlayer charge transfer due to exciton condensation in an electrically isolated gaas quantum well bilayer, *Applied Physics Letters* **118**, 202110 (2021).
- [60] Z. Zhang, E. C. Regan, D. Wang, W. Zhao, S. Wang, M. Sayyad, K. Yumigeta, K. Watanabe, T. Taniguchi, S. Tongay, M. Crommie, A. Zettl, M. P. Zaletel, and F. Wang, Correlated interlayer exciton insulator in double layers of monolayer wse₂ and moiré ws₂/wse₂ (2021), [arXiv:2108.07131 \[cond-mat.mes-hall\]](https://arxiv.org/abs/2108.07131).
- [61] J. Towns, T. Cockerill, M. Dahan, I. Foster, K. Gaither, A. Grimshaw, V. Hazlewood, S. Lathrop, D. Lifka, G. D. Peterson, R. Roskies, J. R. Scott, and N. Wilkins-Diehr, Xsede: Accelerating scientific discovery, *Computing in Science & Engineering* **16**, 62 (2014).
- [62] A. Lau, T. Hyart, C. Autieri, A. Chen, and D. I. Pikulin, Designing three-dimensional flat bands in nodal-line semimetals, *Phys. Rev. X* **11**, 031017 (2021).
- [63] R. Côté, L. Brey, and A. H. MacDonald, Broken-symmetry ground states for the two-dimensional electron gas in a double-quantum-well system, *Phys. Rev. B* **46**, 10239 (1992).
- [64] X.-W. Luo and C. Zhang, Spin-twisted optical lattices: Tunable flat bands and larkin-ovchinnikov superfluids, *Phys. Rev. Lett.* **126**, 103201 (2021).
- [65] H. J. Monkhorst and J. D. Pack, Special points for brillouin-zone integrations, *Phys. Rev. B* **13**, 5188 (1976).

SUPPLEMENTAL MATERIAL

I. MOMENTUM SPACE TIGHT-BINDING MODEL

For all the calculations of TBLG in this paper, we adopt the model introduced by Bistrizer-MacDonald [S1, S2], which is an effective tight-binding model in momentum-space (see Fig. S1). The Dirac points in each layer form a triangular lattice with the reciprocal basis vectors

$$\mathbf{b}_1 = (\sqrt{3}Q, 0), \quad (\text{S1})$$

and

$$\mathbf{b}_2 = (\sqrt{3}Q/2, 3Q/2). \quad (\text{S2})$$

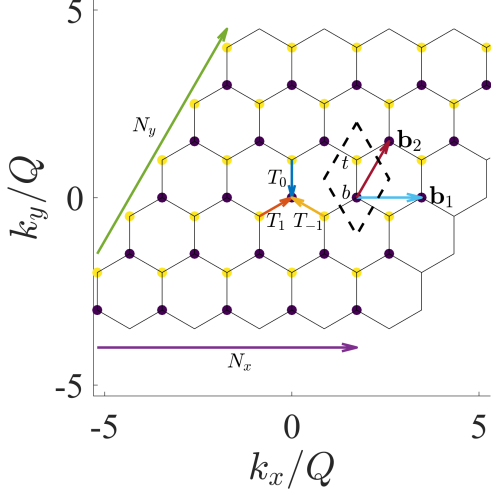


FIG. S1. The Dirac points in each layer form a triangular lattice with basis vectors \mathbf{b}_1 and \mathbf{b}_2 . Because the momenta of the Dirac points in the two layers are shifted by $\beta_+ = (0, 0)$ and $\beta_- = (0, Q)$, we obtain a honeycomb lattice of Dirac points coupled by matrices T_j describing the tunneling between the layers. N_x and N_y are the number of primitive cells, along the \mathbf{b}_1 , \mathbf{b}_2 direction, respectively, forming the lattice.

where $Q = 8\pi \sin(\theta/2)/3a_0$, a_0 is the lattice constant for graphene and θ is the twist angle. The Dirac points in the two layers are shifted relative to each other by $\beta_+ = (0, 0)$ and $\beta_- = (0, Q)$, so that we end up with an effective honeycomb lattice. The onsite block at each lattice site \mathbf{b} , corresponding to the \mathbf{K} valley of the graphene sheets, is described by the Hamiltonian

$$H_{\mathbf{K}\mathbf{b}}^{(t/b)}(\mathbf{k}) = e^{\mp i\frac{\theta}{4}\sigma_z} [\hbar v_F(\mathbf{k} - \boldsymbol{\kappa}_{\mathbf{b}\pm}) \cdot \boldsymbol{\sigma} - \mu\sigma_0] e^{\pm i\frac{\theta}{4}\sigma_z}, \quad (\text{S3})$$

where the first (second) sign is associated to the bottom (top), i.e. b , (t), graphene sheet, σ_i are Pauli matrices in sublattice A/B space, $v_F = 10^6$ m/s is the Fermi velocity in graphene, \mathbf{k} is the electron wave vector (measured from \mathbf{K}), $\boldsymbol{\kappa}_{\mathbf{b}\pm} = \mathbf{b} + \beta_{\pm}$, and μ is the chemical potential. The matrices $T_j = w[\tau_0 + \cos(2\pi j/3)\tau_x + \sin(2\pi j/3)\tau_y]$ [S1, S2], with $j = -1, 0, 1$, describe tunneling processes between nearest neighbors on the lattice sites built in momentum space, see Fig. S1. $H_{\mathbf{K}'}$ is obtained from $H_{\mathbf{K}}$ via time reversal. We assume $w = 118$ meV [S3, S4].

For the determination of the phase diagram and the stiffness calculations, we use lattices with $N_x = 11$ and $N_y = 11$ primitive cells along the \mathbf{b}_1 and \mathbf{b}_2 directions, respectively, resulting in $2N_x N_y = 242$ momentum-space lattice points. To solve the non-linear gap equations we consider the momentum-space unit-cells with $|\mathbf{b}| \leq 5|\mathbf{b}_1|$, which corresponds to $2 \times 91 = 182$ momentum-space lattice points. We have verified that both sets of momentum-space lattice points give the same results and that are sufficiently large that the results do not change if the number of momentum-space lattice

points is further increased.

II. JUSTIFICATION OF LOCAL-INTERACTION APPROXIMATION

In this section we justify the local-interaction approximation that we have used to obtain the mean-field equations. Let's consider the exciton order parameter $\Delta(\mathbf{k})$ assuming that the spin- and valley-rotation symmetries are satisfied, so that we can neglect these degrees of freedom in our analysis. Then the mean field Hamiltonian projected to the lowest energy bands of the two TBLGs (denoted U and L) is given by

$$H_{\text{MF}} = \sum_{\mathbf{k}} c_{\mathbf{k}}^\dagger \begin{pmatrix} \xi_0(\mathbf{k}) + \xi_z(\mathbf{k}) & \Delta(\mathbf{k}) \\ \Delta(\mathbf{k}) & \xi_0(\mathbf{k}) - \xi_z(\mathbf{k}) \end{pmatrix} c_{\mathbf{k}}, \quad (\text{S4})$$

where $c_{\mathbf{k}}^\dagger = (c_{U,\mathbf{k}}^\dagger, c_{L,\mathbf{k}}^\dagger)$, $\xi_0(\mathbf{k}) \pm \xi_z(\mathbf{k})$ are the normal state dispersions in the U/L layers,

$$\Delta(\mathbf{k}) = \sum_{\mathbf{k}'} V(\mathbf{k}, \mathbf{k}') \frac{\Delta(\mathbf{k}')}{2\sqrt{\xi_z^2(\mathbf{k}') + \Delta^2(\mathbf{k}')}} \begin{bmatrix} n_F(-\sqrt{\xi_z^2(\mathbf{k}') + \Delta^2(\mathbf{k}')} + \xi_0(\mathbf{k})) \\ -n_F(\sqrt{\xi_z^2(\mathbf{k}') + \Delta^2(\mathbf{k}')} + \xi_0(\mathbf{k})) \end{bmatrix}, \quad (\text{S5})$$

and $V(\mathbf{k}, \mathbf{k}')$ describes the electron-electron interactions projected to the lowest bands. Close to the critical temperature this gap equation can be linearized giving

$$\Delta(\mathbf{k}) = \sum_{\mathbf{k}'} V(\mathbf{k}, \mathbf{k}') \frac{\Delta(\mathbf{k}')}{2|\xi_z(\mathbf{k}')|} \left[n_F(-|\xi_z(\mathbf{k}')| + \xi_0(\mathbf{k})) - n_F(|\xi_z(\mathbf{k}')| + \xi_0(\mathbf{k})) \right]. \quad (\text{S6})$$

In general, the exciton order parameter is momentum-dependent due to the dispersion of the bands. However, if we assume that the dispersions of the bands are approximately flat we can neglect the momentum-dependence of $\Delta(\mathbf{k})$. Then the non-linear and linear gap equations take the forms

$$\Delta = V_{\text{eff}} \frac{\Delta}{2\sqrt{\xi_z^2 + \Delta^2}} \left[n_F(-\sqrt{\xi_z^2 + \Delta^2} + \xi_0) - n_F(\sqrt{\xi_z^2 + \Delta^2} + \xi_0) \right], \quad (\text{S7})$$

and

$$\Delta = V_{\text{eff}} \frac{\Delta}{2|\xi_z|} \left[n_F(-|\xi_z| + \xi_0) - n_F(|\xi_z| + \xi_0) \right], \quad (\text{S8})$$

respectively, where

$$V_{\text{eff}} = \sum_{\mathbf{k}'} V(\mathbf{k}, \mathbf{k}'). \quad (\text{S9})$$

This means that in both cases we can replace the interactions with a momentum-independent effective interaction strength

V_{eff} so that neither the critical temperature obtained from the linearized gap equations, nor the order parameter obtained from the full non-linear gap equations is affected by the detailed momentum dependence of the interactions.

Following the analysis above, it can be shown that also to calculate the superconducting and magnetic order parameters the interaction is well approximated by an effective local interaction. In general, in systems with sufficiently flat bands, local and long-range interactions will yield similar results. This has been utilized in numerous works related to symmetry-broken states in quantum Hall bilayers, see e.g. Ref. [S5, S6], where it was shown that the long-range Coulomb interactions can be replaced by effective local interactions with interaction strength $V_c \sim e^2/(4\pi\epsilon\epsilon_0 l_B)$, where l_B is the magnetic length describing the distance between the particles. Moreover, a similar projection of the interactions to the flat bands has been used to replace the momentum-dependent Coulomb repulsion, and the phonon-mediated attraction, with momentum-independent effective interaction strengths in other flat-band systems [S7, S8].

Given that in TBLG the low energy bands are very flat the local-interactions approximation is quite accurate. It might be worth pointing out that our results, obtained using the local-interactions approximation, are in agreement with the mean-field results obtained in Ref. [S9], where the long-range Coulomb interactions were used. Our results are also qualitatively consistent with the experimentally observed doping dependence of the competition of the superconducting and correlated insulating phases. One situation when, for TBLG, the local-interaction approximation would not be valid is the case when the translational symmetry of the moiré superlattice is spontaneously broken due to a finite momentum pairing, or charge density wave, or spin density wave order. In these cases, the comparison of the energies of the candidate ground states would require us to take into account the momentum-dependence of the interactions. However, to our knowledge, there is no evidence of spontaneously broken translational symmetry of the moiré superlattice in TBLGs so far, and that is not a situation that we consider in the current work. In quantum Hall exciton condensates, it is known that the order parameters can spontaneously break the translational symmetry if the distance between the layers is larger than the distance between the particles within the layer [S10]. In our case, the distance between the layers can be just few atomic constants because the insulating layer can be made out of h-BN or WSe₂ having a very large insulating gap. Therefore, we do not expect that phases with spontaneously broken translational symmetry will appear in our system.

III. PHASE DIAGRAM FOR AN IDEAL FLAT-BAND MODEL

To get insights into the form of the phase diagram we can assume the bands to be completely flat. This is a rough approximation, but it is sufficient to identify the main qualitative

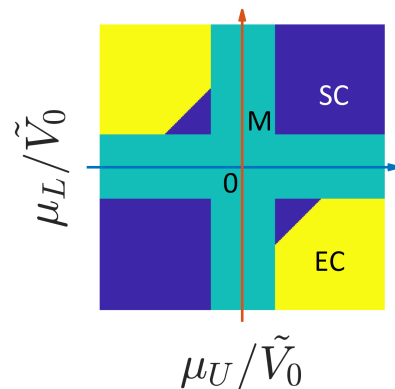


FIG. S2. Phase diagram of a double layer system with ideal flat bands, here \tilde{V}_0 : effective interaction strength for the correlated insulator states.

features of the phase diagram. Almost flat bands can not only be obtained in systems formed by two two-dimensional crystal stacked with a relative twist, but can also be realized in optical lattices [S11]. In the limit in which the bands are completely flat the non-interacting Hamiltonian can be written as

$$H_{\text{flat}} = -\mu_U \sum_{ks} c_{ksU}^\dagger c_{ksU} - \mu_L \sum_{ks} c_{ksL}^\dagger c_{ksL}, \quad (\text{S10})$$

where s represents a spin or orbital degree of freedom.

As discussed in the main text: (i) close to half-filling $\mu_U = \mu_L = 0$ we expect an intralayer correlated state, (ii) for $\mu_U = \mu_L$ and $|\mu_U|$ sufficiently large we expect a superconducting state, (iii) for $\mu_U = -\mu_L$, and $|\mu_U|$ sufficiently large, we expect an exciton condensate state [Fig. 1(b) in the main text]. In this section we show that this expectation can be confirmed with a simple analysis based on the structure of the gap equations resembling the approach used in Ref. [S12]. We describe the gap equations for each type of symmetry-broken state separately, and then use them to study the competition between the phases.

The gap equation for s -wave superconductivity in each layer is (we can assume that superconducting pairing in each layer occurs independently)

$$\begin{aligned} \Delta_{SC,T} &= \frac{V_{SC}}{2} \frac{\Delta_{SC,T}}{\sqrt{\mu_T^2 + \Delta_{SC,T}^2}} \left[n_F(-\sqrt{\Delta_{SC,T}^2 + \mu_T^2}) \right. \\ &\quad \left. - n_F(\sqrt{\Delta_{SC,T}^2 + \mu_T^2}) \right] \\ &= \frac{V_{SC}}{2} \frac{\Delta_{SC,T}}{\sqrt{\mu_T^2 + \Delta_{SC,T}^2}} \tanh(\beta \sqrt{\Delta_{SC,T}^2 + \mu_T^2}/2), \end{aligned} \quad (\text{S11})$$

where $n_F(E)$ is the Fermi function, V_{SC} is the effective interaction strength for superconductivity obtained by projecting the true interactions into the eigenstates of the flat-band system, μ_T ($T = U, L$) is the chemical potential in each layer,

$\Delta_{SC,T}$ is the superconducting order parameter in each layer, $\beta = 1/(k_B T_0)$ and T_0 is the temperature. The critical temperature $T_{SC,T,c}$ for the superconducting state is given by

$$k_B T_{SC,T,c} = \frac{\mu_T}{2 \operatorname{arctanh}(2\mu_T/V_{SC})}. \quad (\text{S12})$$

The largest critical temperature $k_B T_{SC,T,c} = V_{SC}/4$ is obtained for $\mu_T = 0$.

For an intralayer symmetry-broken state (say for magnetism) the gap equation is

$$\begin{aligned} m_T &= \frac{\tilde{V}_0}{2} \left[n_F(-m_T - \mu_T) - n_F(m_T - \mu_T) \right] \\ &= \frac{\tilde{V}_0}{2} \frac{\sinh \beta m_T}{\cosh \beta \mu_T + \cosh \beta m_T}, \end{aligned} \quad (\text{S13})$$

where \tilde{V}_0 is the effective interaction strength for intralayer interactions and m_T is the order parameter of the intralayer symmetry-broken state. The critical temperature of the intralayer correlated state is determined by the equation

$$k_B T_{0,T,c} \left[\cosh(\mu_T/k_B T_{0,T,c}) + 1 \right] = \frac{\tilde{V}_0}{2}. \quad (\text{S14})$$

The largest critical temperature $k_B T_{0,T,c} = \tilde{V}_0/4$ is obtained for $\mu_T = 0$.

For an exciton condensate state the gap equation is

$$\begin{aligned} \Delta_{EC} &= \frac{V_{EC}}{2} \frac{\Delta_{EC}}{\sqrt{\mu_{as}^2 + \Delta_{EC}^2}} \left[n_F \left(-\sqrt{\Delta_{EC}^2 + \mu_{as}^2} - \mu_s \right) \right. \\ &\quad \left. - n_F \left(\sqrt{\Delta_{EC}^2 + \mu_{as}^2} - \mu_s \right) \right] \\ &= \frac{V_{EC}}{2} \frac{\Delta_{EC}}{\sqrt{\mu_{as}^2 + \Delta_{EC}^2}} \\ &\quad \times \frac{\sinh \left(\beta \sqrt{\mu_{as}^2 + \Delta_{EC}^2} \right)}{\cosh \beta \mu_s + \cosh \left(\beta \sqrt{\mu_{as}^2 + \Delta_{EC}^2} \right)}, \end{aligned} \quad (\text{S15})$$

where V_{EC} is the effective interaction strength for exciton condensation, $\mu_s = (\mu_U + \mu_L)/2$ and $\mu_{as} = (\mu_U - \mu_L)/2$. If we have balanced electron and hole densities $\mu_U = -\mu_L$ the gap equation for the exciton condensation has the same form as in the case of superconductivity. If the layers have equal densities of similar type of carriers $\mu_U = \mu_L$ the gap equation for the exciton condensation takes the same form as in the case of intralayer correlated state. The critical temperature for the exciton condensation is determined by the equation

$$\frac{\sinh(\mu_{as}/k_B T_{EC,c})}{\cosh(\mu_s/k_B T_{EC,c}) + \cosh(\mu_{as}/k_B T_{EC,c})} = \frac{2\mu_{as}}{V_{EC}}. \quad (\text{S16})$$

If $\mu_s = 0$ we obtain

$$k_B T_{EC,c} = \frac{\mu_{as}}{2 \operatorname{arctanh}(2\mu_{as}/V_{EC})}, \quad (\text{S17})$$

resembling the equation for critical temperature of superconductivity but with chemical potential replaced by the layer

asymmetric chemical potential $\mu_{as} = (\mu_U - \mu_L)/2$. If $\mu_{as} = 0$ we obtain

$$k_B T_{EC,c} \left[\cosh(\mu_s/k_B T_{EC,c}) + 1 \right] = \frac{V_{EC}}{2} \quad (\text{S18})$$

resembling the equation for critical temperature of intralayer correlated state but with chemical potential replaced by the layer symmetric chemical potential $\mu_s = (\mu_U + \mu_L)/2$. The largest critical temperature $k_B T_{EC,c} = V_{EC}/4$ is obtained for $\mu_U = \mu_L = 0$.

To describe the competition between different phases as a function of μ_U and μ_L we use the following procedure: For each μ_U and μ_L we solve the critical temperatures for the superconductivity from Eq. (S12) (taking the larger value from $T_{SC,U,c}$ and $T_{SC,L,c}$), intralayer correlated states from Eq. (S14) (taking the larger value from $T_{0,U,c}$ and $T_{0,L,c}$) and exciton condensation from Eq. (S16). We assume that the phase which is realized at each μ_U and μ_L is the one with the largest critical temperature.

We assume that the interaction constants satisfy the realistic hierarchy $\tilde{V}_0 > V_{EC} \sim V_{SC}$. Knowing that superconductivity can be easily realized in twisted bilayer graphene we can expect V_{SC} to be not much smaller than \tilde{V}_0 . As an example, Fig. S2 shows the phase diagram obtained assuming $\tilde{V}_0 = 162\text{meV}$, $V_{EC} = 0.8\tilde{V}_0$ and $V_{SC} = 0.6\tilde{V}_0$. We see that in this case, as expected, we obtain the phase diagram discussed at the beginning of this section. We emphasize that the overall structure of this phase diagram is a universal consequence of the structure of the gap equations, and arises independently of the details of the microscopic model.

IV. THE DETERMINATION OF THE PHASE DIAGRAM FROM THE LINEARIZED GAP EQUATIONS

In this section, we describe the approach used to obtain the phase diagram using the linearized gap equations obtained using the full TBLG bands, and provide the full expression of such equations. As in the main text, we consider three different phases: exciton condensate (EC), superconductivity (SC), and orbital magnetism (OM).

To obtain the phase diagram, for each pair of values in the (μ_U, μ_L) plane we calculate the transition temperature (T_c) for each phase, and then identify the phase of the ground state as the one with the largest T_c . As we discussed in the next section, we have verified for several sample points in the (μ_U, μ_L) plane that the phase with the largest T_c is the ground state phase (i.e. the phase at zero temperature) by solving the full non-linear gap equation, allowing also for the possibility of coexistence of different phases.

For the EC phase the linearized gap equation takes the form:

$$\Delta_{\mathbf{b}_1 l_1 \sigma_1 l'_1 \sigma'_1}^{\text{EC}} = \sum_{\mathbf{b}_2 l_2 \sigma_2 l'_2 \sigma'_2} \chi_{\mathbf{b}_1 \mathbf{b}_2}^{l_1 \sigma_1 l'_1 \sigma'_1; l_2 \sigma_2 l'_2 \sigma'_2} \Delta_{\mathbf{b}_2 l_2 \sigma_2 l'_2 \sigma'_2}^{\text{EC}}, \quad (\text{S19})$$

where

$$\chi_{\mathbf{b}_1\mathbf{b}_2}^{l_1\sigma_1l'_1\sigma'_1;l_2\sigma_2l'_2\sigma'_2} = \frac{V_{\text{EC}}}{\mathcal{A}} \sum_{\substack{n_1n_2 \\ bb'q}} \frac{n_F[\xi_{n_2L}(\mathbf{q})] - n_F[\xi_{n_1U}(\mathbf{q})]}{\xi_{n_1U}(\mathbf{q}) - \xi_{n_2L}(\mathbf{q})} \\ u_{n_1\mathbf{b}_1+\mathbf{b}_2l_1\sigma_1U}(\mathbf{q})u_{n_2\mathbf{b}'_1l'_1\sigma'_1L}^*(\mathbf{q}) \\ u_{n_1\mathbf{b}'_1+\mathbf{b}_2l_2\sigma_2U}^*(\mathbf{q})u_{n_2\mathbf{b}'_2l'_2\sigma'_2L}(\mathbf{q}), \quad (\text{S20})$$

is the pairing susceptibility, V_{EC} is the interaction strength for the EC phase, \mathcal{A} is the area of the sample, $u_{n\mathbf{b}l\sigma T}(\mathbf{q})$ is the component of the non-interacting wave function for a single upper ($T = U$) or lower ($T = L$) TBLG with reciprocal basis vector \mathbf{b} , layer l , sublattice σ , and band index n . Here $\xi_{U,L}(\mathbf{q}) = \epsilon_{\mathbf{q}} - \mu_{U,L}$, with $\epsilon_{\mathbf{q}}$ the non-interacting energy eigenvalue.

For the superconducting case, we assume the pairing to be s -wave, and sublattice independent so that for each TBLG we have the linearized gap equation [S2]:

$$\Delta_{\mathbf{b}l}^{\text{SC}} = \sum_{\mathbf{b}'l'} \chi_{\mathbf{b}l,\mathbf{b}'l'}^{\text{SC}} \Delta_{\mathbf{b}'l'}^{\text{SC}}, \quad (\text{S21})$$

with

$$\chi_{\mathbf{b}l,\mathbf{b}'l'}^{\text{SC}} = \frac{V_{\text{SC}}}{2\mathcal{A}} \sum_{nmq} \frac{1 - n_F(\xi_{n\mathbf{q}}) - n_F(\xi_{m\mathbf{q}})}{\xi_{n\mathbf{q}} + \xi_{m\mathbf{q}}} \\ [\langle u_{n\mathbf{q}} | u_{m\mathbf{q}} \rangle_{\mathbf{b}l}]^* \langle u_{n\mathbf{q}} | u_{m\mathbf{q}} \rangle_{\mathbf{b}'l'}, \quad (\text{S22})$$

where the 2 in front of \mathcal{A} is due to the summation over sublattices in the $\langle \rangle$ expression, and n, m are band indexes [S2].

Previous work [S9] strongly suggests that the orbital magnetic phase energetically most favored has order parameter $\Delta_{\text{OM}} = \langle \Psi_{GS} | \hat{\sigma}_z | \Psi_{GS} \rangle$ where $|\Psi_{GS}\rangle$ is the ground-state and $\hat{\sigma}_z$ is the z Pauli matrix in sublattice space. For such order parameter we obtain the following linearized-gap equation

$$\Delta_{\mathbf{b}l}^{\text{OM}} = \sum_{\mathbf{b}'l'} \chi_{\mathbf{b}l,\mathbf{b}'l'}^{\text{OM}} \Delta_{\mathbf{b}'l'}^{\text{OM}}, \quad (\text{S23})$$

with

$$\chi_{\mathbf{b}l,\mathbf{b}'l'}^{\text{OM}} = \frac{V_{\text{OM}}}{\mathcal{A}} \sum_{nmq} \frac{n_F(\xi_{n\mathbf{q}}) - n_F(\xi_{m\mathbf{q}})}{\xi_{m\mathbf{q}} - \xi_{n\mathbf{q}}} \\ [\langle u_{n\mathbf{q}A} | \hat{\sigma}_z | u_{m\mathbf{q}A} \rangle_{\mathbf{b}l}]^* \langle u_{n\mathbf{q}A} | \hat{\sigma}_z | u_{m\mathbf{q}A} \rangle_{\mathbf{b}'l'}. \quad (\text{S24})$$

The factor 2 in front of \mathcal{A} on the r.h.s. of Eq. (S24) is cancelled by the factor 2 in front of V_{OM} due to the spin degeneracy.

To obtain the linear response functions we use 60×60 k-points to calculate the sum in momentum space. We have verified that further increasing the number of k-points does not affect the phase diagram.

The number of \mathbf{b} vectors necessary to obtain accurate estimates of T_c depends on the order parameter considered. For superconductivity it is sufficient to keep all the \mathbf{b} vectors with magnitude no larger than $2|\mathbf{b}_1|$, which corresponds to 19 \mathbf{b} vectors [S2].

For the EC order parameters we find that one needs to keep all the \mathbf{b} vectors with $|\mathbf{b}| \leq 3|\mathbf{b}_1|$, i.e. a total of 37 \mathbf{b} vectors. This is shown in Fig. S3, and is consistent with the fact

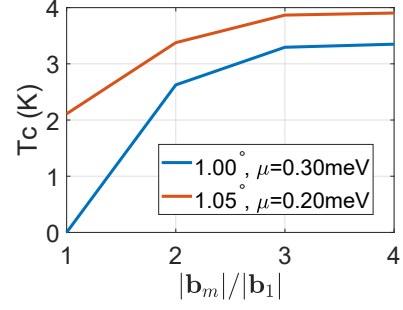


FIG. S3. T_c for the EC phase as a function of the magnitude of the largest \mathbf{b} vectors kept in solving the linearized gap equation. The numbers of \mathbf{b} vectors are respectively 7, 19, 37, 61 with $|\mathbf{b}_m/\mathbf{b}_1|$ increased from 1 to 4.

that the EC phase is characterized by a multi-component order parameter requiring more momentum states to accurately describe it. Similar arguments and results apply to the OM phase. Consequently, all the results presented in the main text, and in the remainder, were obtained by keeping all the \mathbf{b} with $|\mathbf{b}| \leq 4|\mathbf{b}_1|$ resulting in a total of 61 \mathbf{b} vectors.

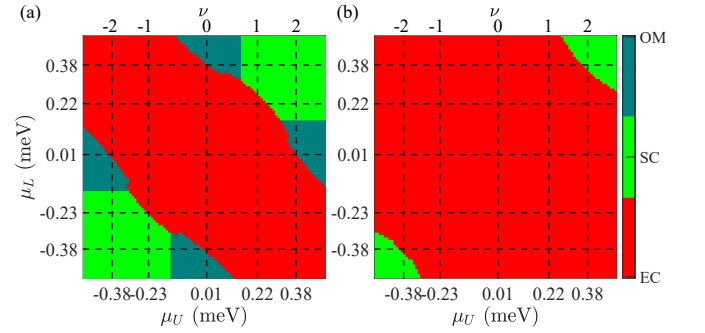


FIG. S4. Effect of V_{EC} on the phase diagram. For both panels: $\theta = 1.00^\circ$, $V_{\text{SC}} = 75 \text{ meV}\cdot\text{nm}^2$, and $V_{\text{OM}} = 130 \text{ meV}\cdot\text{nm}^2$, the same values used for Fig. 1 (b) in the main text. However for (a) $V_{\text{EC}} = 80 \text{ meV}\cdot\text{nm}^2$, and for (b) $V_{\text{EC}} = 100 \text{ meV}\cdot\text{nm}^2$, whereas in Fig. 1 (b) in the main text $V_{\text{EC}} = 60 \text{ meV}\cdot\text{nm}^2$.

Figure 1 (b) in the main text, and Fig. S4 show the phase diagrams obtained using the linearized gap equations with the full TBLG bands, as described above. We see that the phase diagrams obtained using the TBLGs' bands, and realistic values of the interaction strengths exhibit some qualitative differences compared to the phase diagram shown in Fig. S2 obtained using the ideal flat-band model. Figure S4 (a) shows that when $V_{\text{EC}} = 80 \text{ meV}\cdot\text{nm}^2$ the region where the EC dominates is almost two thirds of the total area of the (μ_L, μ_U) plane considered, area that corresponds to filling factors ranging from -2.5 to +2.5 for the moiré supercell. When $V_{\text{EC}} = 100 \text{ meV}\cdot\text{nm}^2$, the EC phase completely pre-

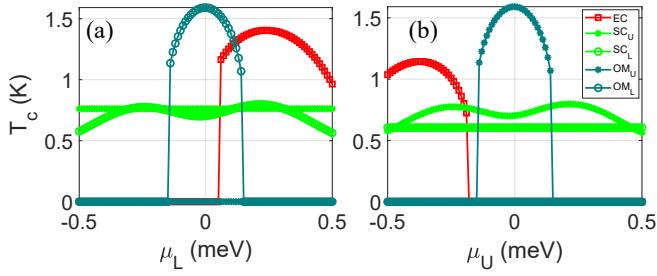


FIG. S5. (a) T_c as a function of μ_L for $\mu_U = -0.3$ meV, the value used for Fig. 1(c) in the main text. (b) T_c as a function of μ_U for $\mu_L = 0.46$ meV, the value used for Fig. 1(d) in the main text. For both plots: $\theta = 1.00^\circ$, $V_{EC} = 60$ meV \cdot nm 2 , $V_{SC} = 75$ meV \cdot nm 2 , and $V_{OM} = 130$ meV \cdot nm 2 .

vails over the other two phases.

Figure S5 shows the evolution of T_c for the different phases as a function of doping in one TBLG while the doping in the other TBLG is kept fixed. We see that the SC phase has a finite T_c for all the doping considered, whereas for the EC and OM phase there are range of dopings for which T_c vanishes.

V. STUDY OF PHASE TRANSITIONS USING THE NON-LINEAR GAP EQUATIONS

To investigate the possibility that different order might co-exist at low temperature it is necessary to obtain the solution of the full non-linear gap equations in which all the order parameters are present and treated on the same footing.

The general form of the mean-field Hamiltonian with all the three phases (EC, SC, OM) allowed is:

$$H = \sum_{\mathbf{k}} \psi_{\mathbf{k}}^\dagger [h_0(\mathbf{k}) + h_1(\mathbf{k})] \psi_{\mathbf{k}}, \quad (\text{S25})$$

where

$$\psi_{\mathbf{k}} = (\phi_{\mathbf{K}+\mathbf{k}U\uparrow}, \phi_{\mathbf{K}+\mathbf{k}L\uparrow}, \phi_{-\mathbf{K}-\mathbf{k}U\downarrow}^\dagger, \phi_{-\mathbf{K}-\mathbf{k}L\downarrow}^\dagger)^T, \quad (\text{S26})$$

with

$$\begin{aligned} \phi_{\mathbf{k}} = & (c_{\mathbf{k}+\mathbf{b}_1bA}, c_{\mathbf{k}+\mathbf{b}_1bB}, c_{\mathbf{k}+\mathbf{b}_1tA}, c_{\mathbf{k}+\mathbf{b}_1tB}, \\ & c_{\mathbf{k}+\mathbf{b}_2bA}, c_{\mathbf{k}+\mathbf{b}_2bB}, c_{\mathbf{k}+\mathbf{b}_2tA}, c_{\mathbf{k}+\mathbf{b}_2tB}, \\ & c_{\mathbf{k}+\mathbf{b}_3bA}, c_{\mathbf{k}+\mathbf{b}_3bB}, c_{\mathbf{k}+\mathbf{b}_3tA}, c_{\mathbf{k}+\mathbf{b}_3tB}, \dots), \end{aligned} \quad (\text{S27})$$

and

$$\begin{aligned} \phi_{-\mathbf{k}} = & (c_{-\mathbf{k}-\mathbf{b}_1bA}, c_{-\mathbf{k}-\mathbf{b}_1bB}, c_{-\mathbf{k}-\mathbf{b}_1tA}, c_{-\mathbf{k}-\mathbf{b}_1tB}, \\ & c_{-\mathbf{k}-\mathbf{b}_2bA}, c_{-\mathbf{k}-\mathbf{b}_2bB}, c_{-\mathbf{k}-\mathbf{b}_2tA}, c_{-\mathbf{k}-\mathbf{b}_2tB}, \\ & c_{-\mathbf{k}-\mathbf{b}_3bA}, c_{-\mathbf{k}-\mathbf{b}_3bB}, c_{-\mathbf{k}-\mathbf{b}_3tA}, c_{-\mathbf{k}-\mathbf{b}_3tB}, \dots), \end{aligned} \quad (\text{S28})$$

where \uparrow, \downarrow is the spin index, and $h_0(\mathbf{k})$ is the matrix describing the kinetic energy. To simplify the notation in the remainder

we do the following renaming $\mathbf{k} + \mathbf{K} \rightarrow \mathbf{k}$, $-\mathbf{k} - \mathbf{K} \rightarrow -\mathbf{k}$ in all c and c^\dagger operators. The kernel $h_1(\mathbf{k})$ has the form:

$$h_1(\mathbf{k}) = \begin{pmatrix} \Delta_{OM}^U(\mathbf{k}) & \Delta_{EC}(\mathbf{k}) & \Delta_{SC}^U(\mathbf{k}) & 0 \\ \Delta_{EC}^\dagger(\mathbf{k}) & \Delta_{OM}^L(\mathbf{k}) & 0 & \Delta_{SC}^L(\mathbf{k}) \\ \Delta_{SC}^{U\dagger}(\mathbf{k}) & 0 & -\Delta_{OM}^U(\mathbf{k}) & -\Delta_{EC}(\mathbf{k}) \\ 0 & \Delta_{SC}^{L\dagger}(\mathbf{k}) & -\Delta_{EC}^\dagger(\mathbf{k}) & -\Delta_{OM}^L(\mathbf{k}) \end{pmatrix}. \quad (\text{S29})$$

In Eq. (S29) Δ_{EC} is the order parameter for the EC phase, Δ_{OM}^U (Δ_{OM}^L) is the order parameter for the OM phase in the upper (lower) TBLG, and Δ_{SC}^U (Δ_{SC}^L) is the order parameter for the SC phase in the upper (lower) TBLG.

We assume the EC order parameter to be periodic on the moiré lattice with the Fourier expansion

$$\Delta_{\mathbf{r}l\sigma'l'\sigma'}^{EC} = \sum_b \Delta_{\mathbf{b}l\sigma'l'\sigma'}^{EC} e^{i\mathbf{b}\cdot\mathbf{r}}, \quad (\text{S30})$$

where

$$\Delta_{\mathbf{b}l\sigma'l'\sigma'}^{EC} = -\frac{V_{EC}}{\mathcal{A}} \sum_{k_1 b_2} \langle c_{L\mathbf{k}_1+\mathbf{b}_2l'\sigma'}^\dagger c_{U\mathbf{k}_1+\mathbf{b}_2+\mathbf{b}l\sigma} \rangle. \quad (\text{S31})$$

Via a unitary transformation \mathcal{U} into the bands eigenstates,

$$c_{U\mathbf{k}_1+\mathbf{b}_1l\sigma} = \sum_n \mathcal{U}_{Un\mathbf{k}_1+\mathbf{b}_1}^{l\sigma} c_{n\mathbf{k}_1}, \quad (\text{S32})$$

$$c_{L\mathbf{k}_1+\mathbf{b}_1l\sigma}^\dagger = \sum_n \mathcal{U}_{Ln\mathbf{k}_1+\mathbf{b}_1}^{l\sigma*} c_{n\mathbf{k}_1}^\dagger, \quad (\text{S33})$$

we obtain

$$\Delta_{\mathbf{b}l\sigma'l'\sigma'}^{EC} = -\frac{V_{EC}}{\mathcal{A}} \sum_{k_1 b_2 m} \mathcal{U}_{Lm\mathbf{k}_1+\mathbf{b}_2}^{l'\sigma'*} \mathcal{U}_{Um\mathbf{k}_1+\mathbf{b}_2+\mathbf{b}}^{l\sigma} n_F(E_{m\mathbf{k}_1}), \quad (\text{S34})$$

where $E_{m\mathbf{k}}$ are the eigenvalues of the full Hamiltonian Eq.(S25). We have checked that this equation is equivalent to the linearized gap Eq.(S19) in the small order parameter limit.

For the SC order parameter we have

$$\Delta_{\mathbf{r}l\sigma}^{SC} = \sum_b \Delta_{\mathbf{b}l\sigma}^{SC} e^{i\mathbf{b}\cdot\mathbf{r}}. \quad (\text{S35})$$

Assuming the SC order parameter is sub-lattice independent, i.e. $\Delta_{\mathbf{b}lA}^{SC} = \Delta_{\mathbf{b}lB}^{SC} \equiv \Delta_{\mathbf{b}l}^{SC}$ we obtain

$$\Delta_{\mathbf{b}l}^{SC} = -\frac{V_{SC}}{2\mathcal{A}} \sum_{k_1 b_1 \sigma} \langle c_{-(\mathbf{k}_1+\mathbf{b}_1)l\sigma\downarrow} c_{\mathbf{k}_1+\mathbf{b}_1+\mathbf{b}l\sigma\uparrow} \rangle. \quad (\text{S36})$$

By going into the basis that diagonalizes the full Hamiltonian we have

$$c_{\mathbf{k}_1+\mathbf{b}_1+\mathbf{b}l\sigma\uparrow} = \sum_n \mathcal{U}_{n\mathbf{k}_1+\mathbf{b}_1+\mathbf{b}}^{l\sigma} c_{n\mathbf{k}_1}, \quad (\text{S37})$$

$$c_{-(\mathbf{k}_1+\mathbf{b}_1)l\sigma\downarrow} = \sum_n \mathcal{U}_{n-(\mathbf{k}_1+\mathbf{b}_1)}^{l\sigma*} c_{n\mathbf{k}_1}^\dagger, \quad (\text{S38})$$

and

$$\Delta_{\mathbf{bl}}^{\text{SC}} = -\frac{V_{\text{SC}}}{2\mathcal{A}} \sum_{k_1 b_1 m \sigma} \mathcal{U}_{m-(\mathbf{k}_1+\mathbf{b}_1)\downarrow}^{l\sigma*} \mathcal{U}_{m\mathbf{k}_1+\mathbf{b}_1+\mathbf{b}\uparrow}^{l\sigma} n_F(E_{m\mathbf{k}_1}). \quad (\text{S39})$$

For the OM order parameter we have:

$$\Delta_{\mathbf{bl}}^{\text{OM}} = \frac{V_{\text{OM}}}{\mathcal{A}} \sum_{k_1 b_1 \sigma} \langle c_{\mathbf{k}_1+\mathbf{b}_1 l \sigma}^\dagger \hat{\sigma}_z c_{\mathbf{k}_1+\mathbf{b}_1+\mathbf{b} l \sigma} \rangle_{\bar{0}}, \quad (\text{S40})$$

where $\langle \rangle_{\bar{0}}$ means the expectation value excluding the contribution from the non-interacting ground states. Going into the basis that diagonalizes the full Hamiltonian we obtain:

$$\begin{aligned} \Delta_{\mathbf{bl}}^{\text{OM}} = \frac{V_{\text{OM}}}{\mathcal{A}} \sum_{k_1 b_1 m} [& (\mathcal{U}_{m\mathbf{k}+\mathbf{b}_1 l A}^* \mathcal{U}_{m\mathbf{k}+\mathbf{b}_1+\mathbf{b} l A} \\ & - \mathcal{U}_{m\mathbf{k}+\mathbf{b}_1 l B}^* \mathcal{U}_{m\mathbf{k}+\mathbf{b}_1+\mathbf{b} l B}) n_F(E_{m\mathbf{k}}) \\ & - (\mathcal{U}_{m\mathbf{k}+\mathbf{b}_1 l A}^{0*} \mathcal{U}_{m\mathbf{k}+\mathbf{b}_1+\mathbf{b} l A}^0 \\ & - \mathcal{U}_{m\mathbf{k}+\mathbf{b}_1 l B}^{0*} \mathcal{U}_{m\mathbf{k}+\mathbf{b}_1+\mathbf{b} l B}^0) n_F(\xi_{m\mathbf{k}}^0)], \quad (\text{S41}) \end{aligned}$$

where ξ^0 are the eigenvalues of the non-interacting Hamiltonian matrix h_0 and \mathcal{U}^0 is the unitary transformation that diagonalizes h_0 .

To study the phase transitions along the paths used for Fig.1(c)-(e) in the main text, for each point on such a path, we solve iteratively the non-linear gap equations starting from 30 different, randomly generated, initial states including states for which all the three order parameters are simultaneously non-zero, and states in which only two, or one, order parameters are not zero. In order to guarantee that the calculation is fully unconstrained, for each point on the path, we use different seeds to generate the random initial conditions. We stop the iterative process when, for each component of the order parameters, the difference of the values between two successive iterations is smaller than 5×10^{-4} meV. Among all the solutions obtained from the initial random states, the ground state is identified as the solution for which the total energy per unit cell close to zero temperature

$$\begin{aligned} E_{\text{tot}} = \frac{1}{N} \sum_{n\mathbf{k}} E_{n\mathbf{k}} n_F(E_{n\mathbf{k}}) + \sum_{\mathbf{bl}\sigma l'\sigma' s} \frac{|\Delta_{\mathbf{bl}\sigma l'\sigma'}^{\text{EC}}|^2 \mathcal{A}_0}{V_{\text{EC}}} \\ + \sum_{T\mathbf{bl}\sigma} \frac{|\Delta_{\mathbf{bl}T}^{\text{SC}}|^2 \mathcal{A}_0}{V_{\text{SC}}} + \sum_{T\mathbf{bl}s} \frac{|\Delta_{\mathbf{bl}T}^{\text{OM}}|^2 \mathcal{A}_0}{2V_{\text{OM}}}, \quad (\text{S42}) \end{aligned}$$

is the lowest ($T = (U, L)$ and s is the spin index).

In solving the non-linear gap equation we mesh the Brillouin zone to $2 \times (30 \times 30)$, which is a compromise between speed and precision, with one half of those k-points centering at the origin, and the other half avoiding the high symmetric points in a way similar to the Monkhorst-Pack k-point set [S13]. We have verified that further increasing the sample size or the number of k-meshes only leads to minor changes in the magnitudes of the order parameters.

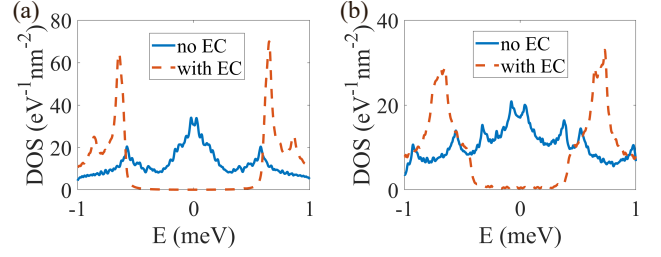


FIG. S6. The density of states without and with exciton condensates. Here the parameters are (a) $\theta = 1.05^\circ$, (b) $\theta = 1.00^\circ$. In both plots $\mu = 0.30$ meV.

VI. NEARLY GAPPED FEATURE OF THE EXCITON CONDENSATE STATE

From the density of states shown in Fig. S6, we can see that although the exciton condensate is a gapless state according to the band structure shown in the main text, the density of states close to the Fermi energy is reduced by more than an order of magnitude in comparison to the normal state. Therefore, in an experiment probing the density of states the transition from normal state to the exciton condensate state would show up as opening of a gap-like feature in the quasiparticle spectrum.

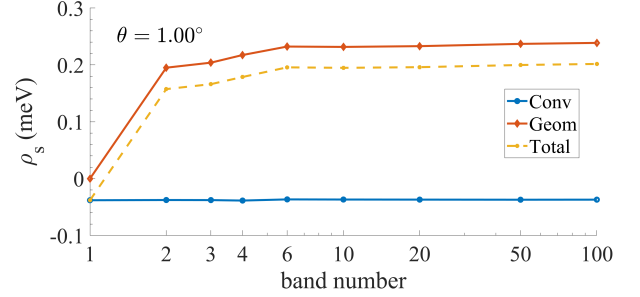


FIG. S7. Here the parameters are $\theta = 1.00^\circ$, and $\mu = 0.30$ meV.

VII. DEPENDENCE OF SUPERFLUID DENSITY ON THE NUMBER OF BANDS INCLUDED IN THE CALCULATION

Because the geometric part in the superfluid density is purely a multiband effect its value can strongly depend on the number of bands included in the calculation. In Fig. S7, one can see that for $\theta = 1.00^\circ$ and $\mu = 0.30$ meV the conventional part of the superfluid density is almost independent of the number of bands included, in contrast to the geometric part. To get accurate results for the geometric part approximately 10 bands need to be included. We have used 10 bands in all the superfluid density calculations reported in the main text.

-
- [S1] R. Bistritzer and A. H. MacDonald, Moire bands in twisted double-layer graphene, *Proceedings of the National Academy of Sciences* **108**, 12233 (2011).
- [S2] F. Wu, A. H. MacDonald, and I. Martin, Theory of Phonon-Mediated Superconductivity in Twisted Bilayer Graphene, *Physical Review Letters* **121**, 257001 (2018).
- [S3] J. Jung, A. Raoux, Z. Qiao, and A. H. MacDonald, Ab initio theory of moiré superlattice bands in layered two-dimensional materials, *Phys. Rev. B* **89**, 205414 (2014).
- [S4] S. Carr, S. Fang, P. Jarillo-Herrero, and E. Kaxiras, Pressure dependence of the magic twist angle in graphene superlattices, *Physical Review B* **98**, 085144 (2018).
- [S5] K. Moon, H. Mori, K. Yang, S. M. Girvin, A. H. MacDonald, L. Zheng, D. Yoshioka, and S.-C. Zhang, Spontaneous interlayer coherence in double-layer quantum hall systems: Charged vortices and kosterlitz-thouless phase transitions, *Phys. Rev. B* **51**, 5138 (1995).
- [S6] D. I. Pikulin, P. G. Silvestrov, and T. Hyart, Confinement-deconfinement transition due to spontaneous symmetry breaking in quantum Hall bilayers, *Nature Communications* **7**, 10462 (2016).
- [S7] R. Ojajärvi, T. Hyart, M. A. Silaev, and T. T. Heikkilä, Competition of electron-phonon mediated superconductivity and Stoner magnetism on a flat band, *Phys. Rev. B* **98**, 054515 (2018).
- [S8] A. Lau, T. Hyart, C. Autieri, A. Chen, and D. I. Pikulin, Designing three-dimensional flat bands in nodal-line semimetals, *Phys. Rev. X* **11**, 031017 (2021).
- [S9] M. Xie and A. H. Macdonald, Nature of the Correlated Insulator States in Twisted Bilayer Graphene, *Physical Review Letters* **124**, 097601 (2020).
- [S10] R. Côté, L. Brey, and A. H. MacDonald, Broken-symmetry ground states for the two-dimensional electron gas in a double-quantum-well system, *Phys. Rev. B* **46**, 10239 (1992).
- [S11] X.-W. Luo and C. Zhang, Spin-twisted optical lattices: Tunable flat bands and larkin-ovchinnikov superfluids, *Phys. Rev. Lett.* **126**, 103201 (2021).
- [S12] T. Löthman and A. M. Black-Schaffer, Universal phase diagrams with superconducting domes for electronic flat bands, *Phys. Rev. B* **96**, 064505 (2017).
- [S13] H. J. Monkhorst and J. D. Pack, Special points for brillouin-zone integrations, *Phys. Rev. B* **13**, 5188 (1976).